The Astrophysical Journal, 677:1385–1394, 2008 April 20 Ⓔ

RHESSI MICROFLARE STATISTICS. I. FLARE-FINDING AND FREQUENCY DISTRIBUTIONS

S. Christe,[1] I. G. Hannah, S. Krucker, J. McTiernan, and R. P. Lin[1]
Space Sciences Laboratory, University of California at Berkeley, Berkeley, CA 94720-7450; schriste@ssl.berkeley.edu,
hannah@ssl.berkeley.edu, krucker@ssl.berkeley.edu, jimm@ssl.berkeley.edu, rlin@ssl.berkeley.edu

Received 2007 September 19; accepted 2007 December 17

ABSTRACT

We present the first in-depth statistical survey of all X-ray microflares observed by *RHESSI* between 2002 March and 2007 March, a total of 25,705 events, an order of magnitude larger then previous studies. These microflares were found using a new flare-finding algorithm designed to search the 6–12 keV count rate when *RHESSI*'s full sensitivity was available in order to find the smallest events. The peak and total count rate are automatically obtained along with count spectra at the peak and the microflare centroid position. Our microflare magnitudes are below *GOES* C class, on average *GOES* A class (background subtracted). They are found to occur only in active regions, not in the "quiet" Sun, and are similar to large flares. The monthly average microflaring rate is found to vary with the solar cycle and ranges from 90 to 5 flares a day during active and quiet times, respectively. Most flares are found to be impulsive (74%), with rise times shorter than decay times. The mean flare duration is ~6 minutes with a 1 minute minimum set by the flare-finding algorithm. The frequency distributions of the peak count rate in the energy bands, 3–6, 6–12, and 12–25 keV, can be represented by power-law distributions with a negative power-law index of 1.50 ± 0.03, 1.51 ± 0.03, and 1.58 ± 0.02, respectively. We find that these power-law indices are constant as a function of time. The X-ray photon spectra for individual events can be approximated with a power-law spectrum $[dJ/d(h\nu) \sim (h\nu)^{-\gamma}]$. Using the ratio of photon fluxes between 10–15 and 15–20 keV, we find $4 < \gamma < 12$, with an average of 7.4. Based on these values, the nonthermal power is calculated. The microflare occurrence frequency varies with the rate of energy release consistent with a power law with an exponent of -1.7 ± 0.1. We estimate the total energy flux deposited in active regions by microflare-associated accelerated electrons (>10 keV) over the five years of observations to be, on average, below 10^{26} erg s^{-1}.

Subject headings: Sun: activity — Sun: corona — Sun: flares — Sun: X-rays, gamma rays

Online material: color figures

1. INTRODUCTION

The Sun releases energy in transient bursts ranging over many orders of magnitude from X-class flares down to microflares. Hard X-ray microflares with nonthermal energies between $\sim 10^{27}$ and 10^{28} erg in electrons with energies greater than 20 keV may occur as often as once every 6 minutes near solar maximum (Lin et al. 1984). Much smaller thermal events have also been observed. The *Yohkoh* soft X-ray telescope (SXT) frequently observed transient brightenings occurring in active regions with energies down to 10^{27} erg (Shimizu 1995). In the "quiet" Sun, outside of active regions, *Yohkoh* SXT, the *Transition Region and Coronal Explorer* (*TRACE*), and the *SOHO* Extreme Ultraviolet Imaging Telescope (EIT) have detected "nanoflares" down to 10^{25} erg (Krucker et al. 1997; Krucker & Benz 1998; Aschwanden et al. 2000; Benz & Krucker 2002). These observations suggest that flares may extend continuously to small energies (we define flares as transient events resulting in significant heating of the local plasma as observed in soft X-rays). Yet discoveries by *Yohkoh* and *TRACE* of other phenomena such as coronal jets suggest that the Sun may impulsively release energy in forms other than flares. The relationship between these transient phenomena and flares is unclear.

Distributions of extensive flare parameters (Crosby et al. 1993; Feldman et al. 1996) are well represented by power laws, suggesting that solar flares may be scale invariant, as suggested by "avalanche" models (Lu & Hamilton 1991; Lu et al. 1993). On the other hand, the discovery (by Lin et al. 2001) that electrons are frequently accelerated to energies well below 25 keV implies that previous flare distributions have underestimated the low-energy cutoff of flare hard X-ray spectra and therefore their nonthermal energies. With *RHESSI* observations, Krucker et al. (2002) and Benz & Grigis (2002) found a similar result but with even more energy due to the fact that *RHESSI* microflares have steeper spectra. Further evidence that large and small flares may be different lies in the occurrence frequency distribution of nanoflares, which may be steeper than for hard X-ray (HXR) flares. Krucker & Benz (1998) and Parnell & Jupp (2000) reported that the nanoflare occurrence-energy frequency distribution was consistent with a negative power-law index of ~2.5 compared to ~1.6 for HXR flares (Crosby et al. 1998). Such a difference between the nanoflare and HXR flare distribution may imply that a break in the flare distribution is necessary in order to bridge the gap between small and large flares and suggests that microflares may be different than large flares.

Determining the flare frequency distribution may be relevant to the coronal heating problem. Parker (1988) suggested that a likely candidate to explain coronal heating was continuous "flaring" at small scales. Thus, there has been much interest in studying the smallest flares. Unfortunately, due to their small energy ($<10^{24}$ erg), Parker's nanoflares remain unobservable. An in-depth statistical study of the smallest HXR flares is therefore necessary in order to determine whether they are similar to large flares and how they are related to coronal heating.

---

[1] Physics Department, University of California at Berkeley, Berkeley, CA 94720-7450.

The *RHESSI* instrument provides uniquely high sensitivity in the energy range of ∼3–15 keV, together with 1 keV FWHM spectral resolution and simultaneous imaging down to $2.3''$ with a full-Sun field of view (Lin et al. 2002), making it ideal for the study of microflares. A number of statistical studies of *RHESSI* flares have already been carried out (Liu et al. 2004; Su et al. 2006; Battaglia et al. 2005; Stoiser et al. 2007; Krucker & Lin 2008). In this series of two papers, we present the first complete statistical survey of microflares observed by *RHESSI*. Here, we concentrate on count rates and flare centroids in order to gain an understanding of *RHESSI* microflares with minimal bias introduced by analysis. The flare-finding algorithm is described in § 2, along with data selection issues. In § 3 we discuss the flaring rate, imaging results, temporal characteristics, and the frequency distribution of count rate. In § 3.4, we present and discuss the flare frequency distribution of the power in accelerated electrons. A second paper (Hannah et al. 2008, hereafter Paper II) focuses on the detailed spectral and imaging analysis of these events.

2. FLARE FINDING

2.1. *Hard X-Ray Observations*

RHESSI consists of nine ultrapure germanium detectors (GeDs), each behind a set of rotation modulation collimators (RMCs) that enable imaging. *RHESSI* achieves its high sensitivity at low energies, compared to previous instruments, through its use of automatic shutters. Most previous instruments used an absorbing window in order to block the excessive thermal fluxes observed in large flares, therefore limiting their observations to energies above ∼20 keV. In *RHESSI's* case, movable shutters are automatically inserted during the high thermal fluxes generated by large flares. With the shutters out, *RHESSI's* sensitivity at 10 keV is up to 100 times higher than that of previous HXR spectrometers (Krucker et al. 2002). High-resolution imaging is achieved with nine RMCs, each consisting of a pair of identical grids made up of slits and slats with different pitches that modulate X-ray sources as the spacecraft rotates, each separate RMC measuring different spatial frequencies. *RHESSI* differs from many imagers in that it records all of the information about each detected photon. This allows for very flexible data analysis, which can be tailored to a specific scientific objective. Summary data are also made available to enable fast data processing. In order to reduce computation time, unless stated otherwise, we have made use of these summary data. Preprocessed 4 s integrated summary data exists for the following energy ranges: 3–6, 6–12, and 12–25 keV. Based on the microflare spectra shown by Krucker et al. (2002) and Benz & Grigis (2002) thermal emission begins to dominate below ∼10 keV; therefore, 3–6 and 6–12 keV are dominated by thermal emission, while 12–25 keV emission is most likely nonthermal.

2.2. *Data Selection*

RHESSI has been operating continuously since 2002 February 12th. Each *RHESSI* orbit provides approximately 1 hr of solar observations followed by about 40 minutes of time spent in eclipse. Solar observations are further reduced by passages through the South Atlantic Anomaly (SAA), during which the detector counts are not recorded due to the high flux of energetic particles. In this article we consider the time period from 2002 March to 2007 March, 5 yr of observations. Due to Earth eclipse and the SAA the actual solar observation time is ∼2.8 yr (1013 days). In order to increase the reliability of automatic flare-finding and maximize the efficiency for finding small flares, only times with shutters out were considered. This requirement limits the number of flares above roughly *GOES* C class (see Fig. 3) and reduces the total observation time by 22% to 768 days. Astrophysical observation campaigns, during which *RHESSI* is off-pointed, further reduce this to 723 days.

2.3. *Flare-Finding Algorithm*

Flares were found through a search for local maxima in the 6–12 keV count rate. Flare fluxes are largest at the lowest energies, but *RHESSI's* sensitivity decreases below ∼5 keV. These two facts and the availability of preprocessed summary data in the 6–12 keV band led to the choice of this energy range. For comparison, the standard *RHESSI* flare list is based on the 12–25 keV range, therefore ignoring weaker events that can often only be seen below 12 keV. The basic algorithm works on the principle that flares are transient signals in time and therefore have a maximum count rate surrounded by regions of positive

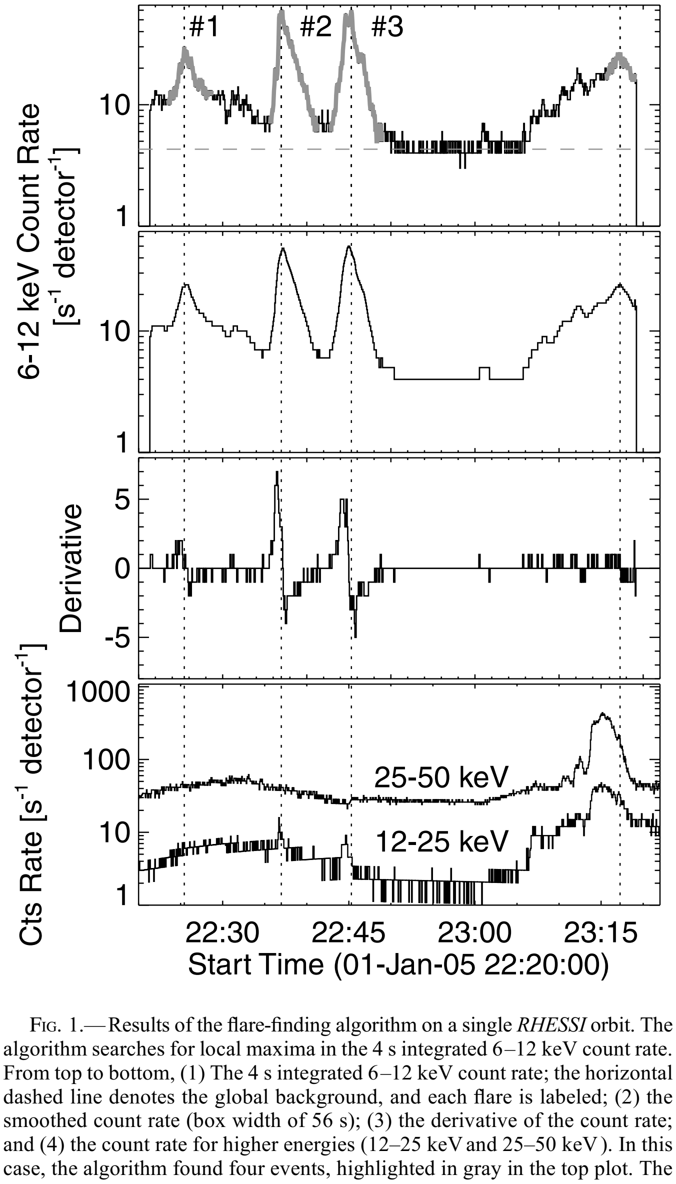

FIG. 1.—Results of the flare-finding algorithm on a single *RHESSI* orbit. The algorithm searches for local maxima in the 4 s integrated 6–12 keV count rate. From top to bottom, (1) The 4 s integrated 6–12 keV count rate; the horizontal dashed line denotes the global background, and each flare is labeled; (2) the smoothed count rate (box width of 56 s); (3) the derivative of the count rate; and (4) the count rate for higher energies (12–25 keV and 25–50 keV). In this case, the algorithm found four events, highlighted in gray in the top plot. The flare-finding algorithm searches for local maxima (*vertical dashed lines*) and then follows the derivative down to the background. Note that the 12–25 keV count rate shows very little or no emission for these events, so they were not included in the standard *RHESSI* flare list. The last event occurred during a particle event (as can be seen in the 12–25 and 25–50 keV count rates) and was discarded.

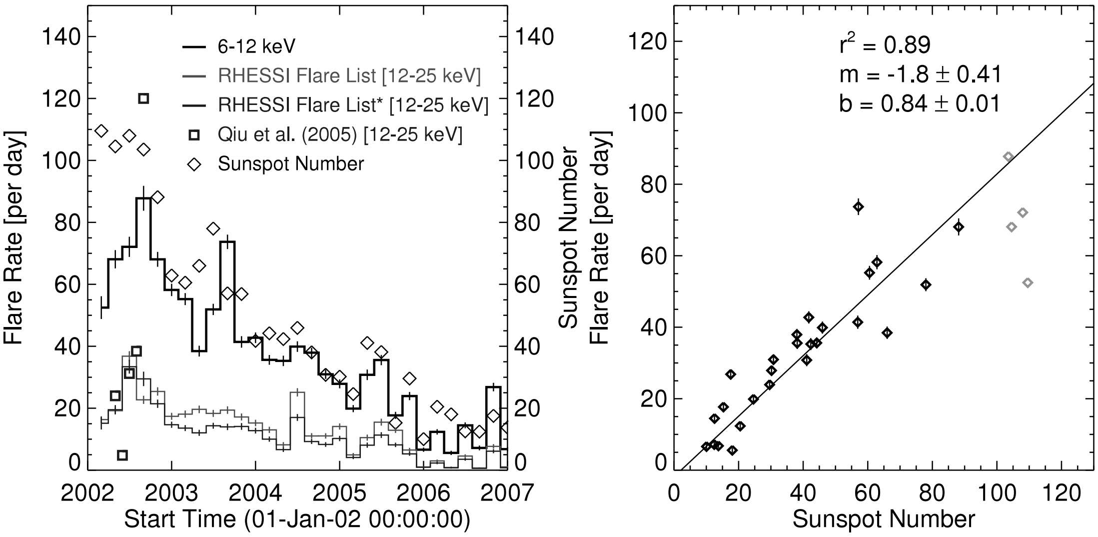

FIG. 2.—*Left*: Flaring rate per day (*left axis*) as a function of time. The average sunspot number is plotted for comparison (*right axis*). The flaring rate is found to vary from ∼90 to 5 flares per day during solar maximum and minimum, respectively. For comparison, the standard *RHESSI* flare list rate is overplotted. The "*RHESSI* flare list*" represents the flare list minus all flares which trigger the shutter. The rates found by Qiu et al. (2004) are also plotted. *Right*: Flare rate plotted versus sunspot number. Due to high solar activity during the first 4 months of the mission, a decreased sensitivity to smaller flares may be present. Those points are plotted in gray. Ignoring those points, a high correlation coefficient was found. A linear fit ($y = mx + b$) to the data is overlaid as well. [*See the electronic edition of the Journal for a color version of this figure.*]

and negative derivatives. Using this fact, an algorithm was designed and its parameters optimized in order to maximize the number of flares found.

The algorithm analyzes individual orbits separately. The 4 s averaged count rate data are smoothed (box width of 56 s), and the derivative is calculated. A local maximum search is then performed, which consists of testing whether at least 40% of the derivative values within an 80 s window on either side of a given maximum value have the correct sign to define a peak. If this is true, then the algorithm follows the slope on either side of the peak until the slope averaged over 40 s is less than 0.1 counts s^{-2}. These values are based on a trial-and-error search of the parameter space in order to maximize the number of events found. The times directly before and after the local maximum are then tested to evaluate whether they are stable background times. In this way, the entire extent of a flare is found, including the rise and decay phase and before- and after-background times. See Figure 1 for an illustration of this method as applied to a *RHESSI* orbit.

The total *RHESSI* orbit is also considered in order to find a global background value. Using this background a test is then performed in order to confirm the statistical significance of each event. The total number of 6–12 keV counts for each event is compared with the total counts in the time-integrated global background of the same duration as the event. We require that the event counts be greater than 3 σ of the noise of the global background counts. Microflares contaminated by particle precipitation events (as flagged by the *RHESSI* summary observations)

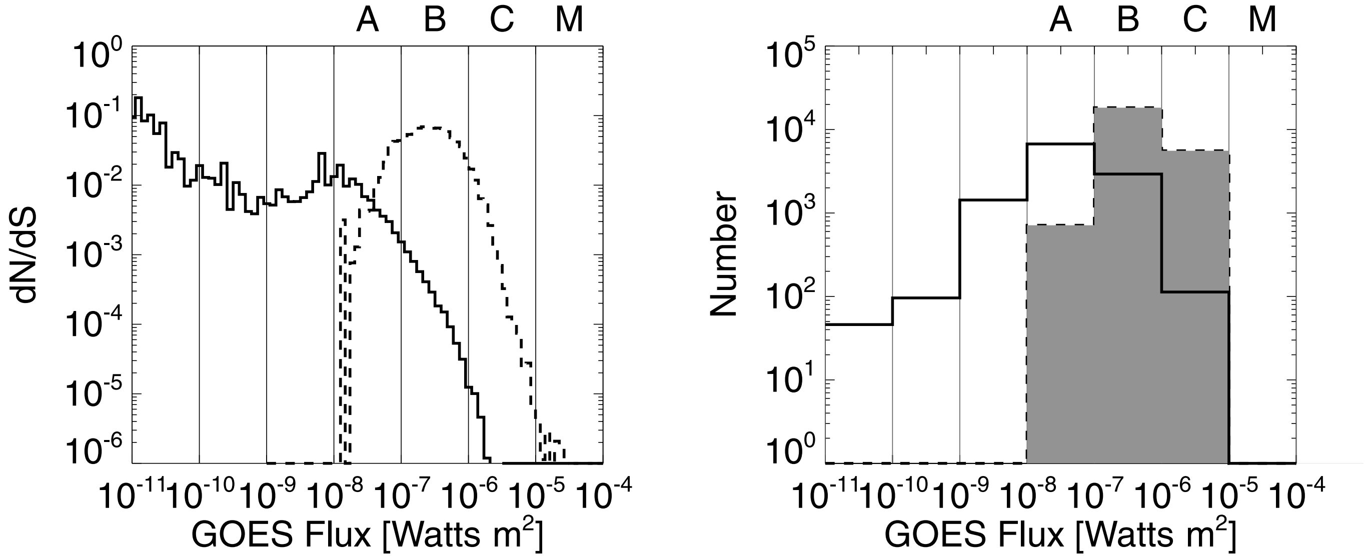

FIG. 3.—*Left*: Histogram of the microflare *GOES* fluxes. The dashed line represents *GOES* fluxes (1–8 Å) at the flare peak as observed by *RHESSI*, while the solid line represents the background-subtracted *GOES* value. The *RHESSI* shutters are normally enabled during large C class flares, setting an upper limit to this distribution. *Right*: Number of flares as a function of *GOES* class. The shaded dashed histogram represents the *GOES* values at the flare peak, and the solid histogram represents the background-subtracted values.

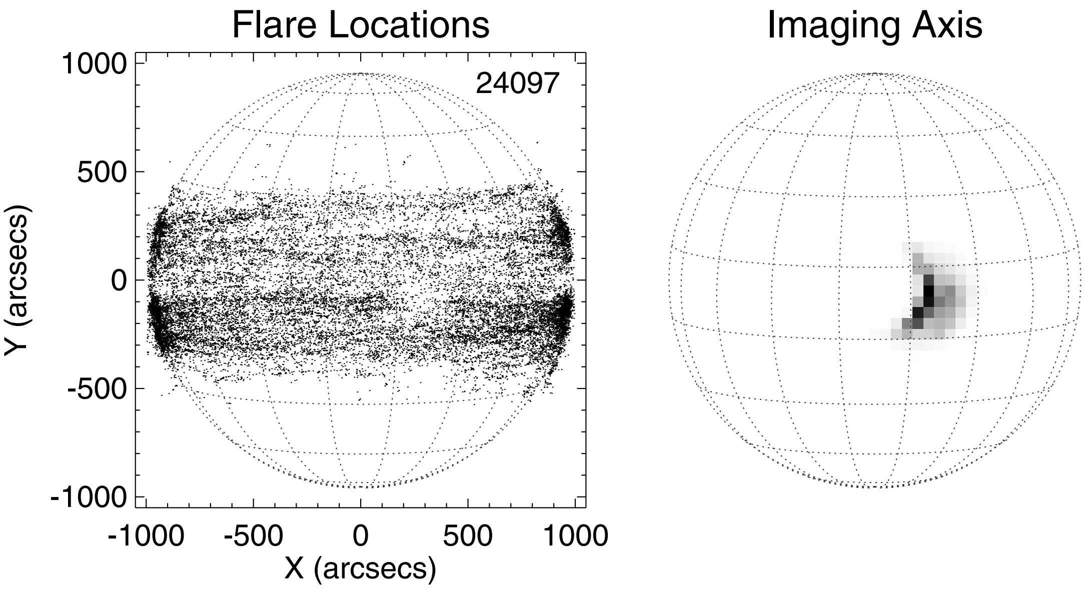

FIG. 4.—*Left*: Flares positions *as observed* plotted on the solar disk. Positions were found by finding the centroid of back-projection images. Flares are concentrated in the active region bands. A clear lack of events can be seen centered around the position of the imaging axis. *Right*: Density plot of the position of the *RHESSI* imaging axis. Flares are not easily imaged in this location due to poor modulation of the flare signal.

are discarded. All flares are also required to have a peak within a single *RHESSI* orbit. This limits the maximum flare duration to $\sim$1 hr. The total number of events found by the flare-finding algorithm that satisfies these requirements is 25,705. In order to certify that events are of solar origin all events are also imaged using back-projection (Hurford et al. 2002) and their locations found (see § 3.1). This requirement reduces the total number of events by 6.2% to 24,097. In comparison, the standard *RHESSI* flare list contains 7268 flares for the same time interval with shutters out. For each flare found, summary data are cataloged including the flare start, peak, and end time, the peak and total count rate, background times and rates both before and after, and observed position.

3. RESULTS

The flaring rate normalized to actual observing time over the total period considered was found to vary from an active time monthly averaged flaring rate of $\sim$90 flares per day ($\sim$1 flare every 16 minutes) down to $\sim$5 flares per day during quiet times. The flaring rate is plotted against time in Figure 2 and is found to decrease as a function of the solar cycle in close correlation with the sunspot number. During the high solar activity of the first 4 months of the mission, we find a low correlation between flare rate and sunspot number. This is due to a decreased sensitivity to small flares due to the occurrence of many large flares, the so-called obscuration effect, as described by Wheatland (2001). For comparison, the flaring rate as found by the *RHESSI* flare list in 12–25 keV is also shown in Figure 2. Only events with good positions were included in this *RHESSI* flare list rate. Our analysis of the *RHESSI* flare list mostly agrees with that of Qiu et al. (2004), who analyzed the same data. Active time event rates are similar to the 3.7 hr^{-1} flaring rate reported by Stoiser et al. (2007). Crosby et al. (1993) studied a complementary set of larger HXR flares (>25 keV) during the previous solar cycle (1980–1990) using *SMM* HXRBS and found the flaring rate varying from $\sim$18 flares per day during active times down to $\sim$1 flare per day during quiet times. The right of Figure 2 shows a scatter plot of the average sunspot number versus flaring rate along with a linear fit to the data. The correlation coefficient between the flaring rate and solar activity is 0.89 if the first 4 months are ignored as discussed above.

Figure 3 shows a histogram of the *GOES* flux for each flare including background-subtracted values. *RHESSI* pre-event background times (see § 2) are used to find an average *GOES* background. The flare sizes are below *GOES* C class, and most flares are *GOES* A class events (background subtracted). The *GOES* flux is approximately power-law distributed. At high *GOES* flux, the distribution falls off due to the fact that large flares are more likely to enable the shutter. This automatically removes them from the microflare list. The trailing off at low *GOES* flux is due to decreasing sensitivity to the smallest events along with a combination of bad background subtraction and the digitization by *GOES* of small events. These microflares are similar in magnitude to those observed by Lin et al. (2001).

3.1. *Flare Positions*

Since all events are imaged in order to confirm their solar origin, flare positions are available for every microflare. The algorithm used to find the flare position is the same as that used for the standard *RHESSI* flare list. Each event found by the algorithm is imaged using the back-projection algorithm (Hurford et al. 2002) at the peak time. If the peak cannot be imaged, then other times within the flare time interval are used. The centroid positions for each RMC image are found and compared. Centroids for at least three RMCs must agree to within $\sim 100''$ for a flare position to be confirmed. If the three largest subcollimators do not agree, then successively smaller ones are used down to subcollimator 5. The average of the consistent values is used as the flare position.

Figure 4 shows all observed heliocentric flare positions on the Sun. Flare positions are concentrated at active region latitudes. The right of Figure 4 shows the average position of *RHESSI*'s imaging axis. Since *RHESSI* imaging depends on modulation of the flare signal, the location of the imaging axis represents an imaging "dead" zone, where the flare signal is only partially modulated. A clear lack of events can be seen around $[250, -100]$, the average location of the imaging axis. Comparing two areas of equal size, one containing the imaging axis and the other not,

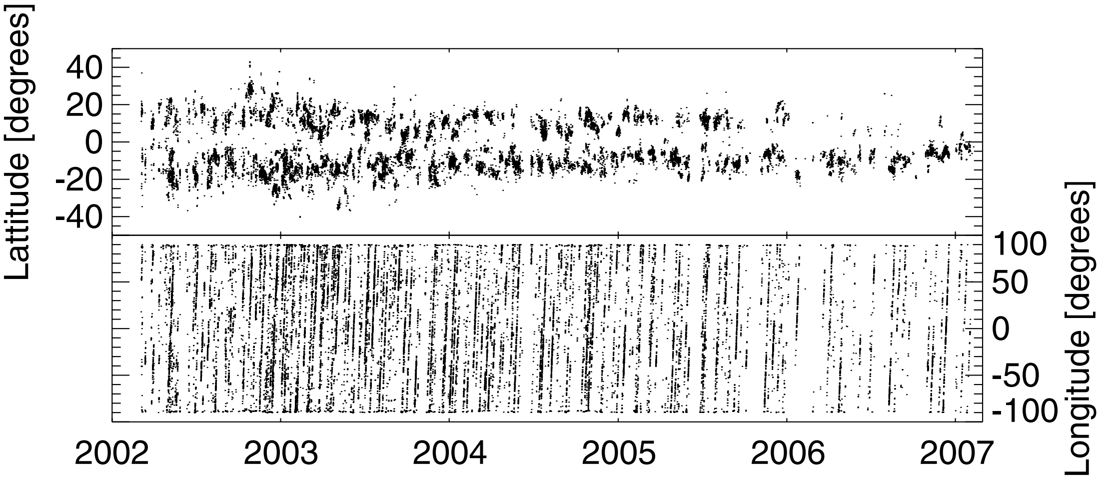

Fig. 5.—Flare latitude (*top*) and longitude (*bottom*). The latitudes are concentrated in the active region bands, while the longitudes show distinct nearly vertical lines. These show repeatedly flaring active regions as they traverse the solar disk.

we estimate that approximately 400 flares were affected by the imaging axis and could not be imaged. The heliographic positions are shown as a function of time in Figure 5. As seen in Figure 4, the flare latitudes are found in the active region bands. Flare latitudes plotted as a function of time suggest a butterfly diagram (Maunder 1904). The flare longitudes show distinct near-vertical features consistent with the motion of repeatedly flaring active regions moving across the solar disk. Figure 6 shows a histogram of the flare latitude and flare radius. The distribution of the latitudes of active regions is also shown for reference. An asymmetry between the total number of flares occurring in the northern and southern solar hemispheres is mirrored by a similar asymmetry in active regions. A similar close relationship between active regions and microflares was also found by Krucker et al. (2002) and more recently by Stoiser et al. (2007). Since flares can occur above the solar limb, the flare longitude is often not relevant and is not shown here. Figure 6 shows a histogram of the microflare radial position normalized to $R_\odot$. We find that 4741 microflares occur above the limb. Most of these over the limb microflares (90%) occur close to the limb at a height of $<0.037\ R_\odot$ (35″ above the limb). Further imaging analysis and results will be presented in a future paper devoted to the subject.

3.2. *Temporal Behavior*

The temporal behavior of flare emission has been previously studied by many authors (e.g., Veronig et al. 2002; Crosby et al. 1993; Bromund et al. 1995) and specific to *RHESSI* by Su et al. (2006). Since our flare-finding algorithm returns the entire extent of a flare, along with the peak time (all found in the thermally dominated 6–12 keV energy range; see § 2), it is possible to consider the total flare duration, as well as the rise time (defined as the time period before the peak, $t_{\rm rise}$) and decay time (defined as the time period after the peak, $t_{\rm decay}$). A histogram of the total flare duration is shown in Figure 7. Note that the flare-finding algorithm sets a minimum threshold of ~1 minute to the flare duration. The mean flare duration is found to be 5.96 minutes. All durations are significantly smaller than the average duration of a *RHESSI* orbit, suggesting that orbital restrictions are not a significant source of bias. Comparing these results with other studies is difficult due to the differing temporal characteristics of thermal (gradual) and nonthermal (impulsive) emission. As was

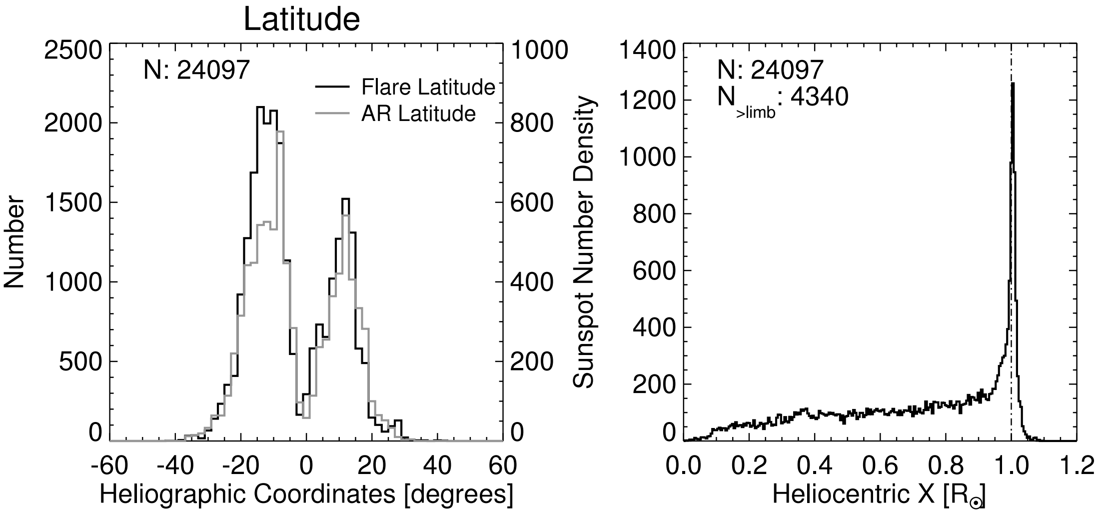

Fig. 6.—Histogram of the heliographic latitude (*left*) and heliocentric radius (*right*) of microflare locations. Flares are observed in the active region latitudes. For comparison, the density of sunspots is also shown. The asymmetry in flare productivity between the northern and southern hemisphere is mirrored in the sunspot density. The distribution of flare heliocentric radii shows that many flares occur above the limb. The lack of events with small radii is caused by the distribution of active regions.

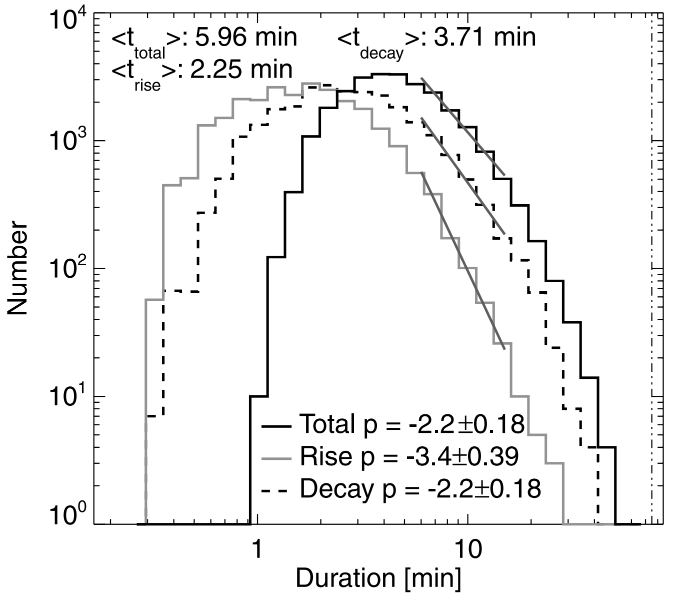

FIG. 7.—Histogram of flare duration. A lower limit of ~1 minute is placed on the flare-finding algorithm while long-duration flares are more likely to trigger the shutters and be excluded from this list. The average total flare duration is ~6 minutes. Overplotted are the rise and decay durations. On average the impulsive duration is shorter than the decay duration. The dot-dashed line marks the average duration of a *RHESSI* orbit.

stated previously (§ 2.1), the 6–12 keV energy range is mostly thermal. Drake (1971) considered an adjacent energy range, 1–6 keV, as detected by *Explorer 33* and *35* and found an average duration of 16 minutes. At similar energies, Veronig et al. (2002) analyzed *GOES* flares and found an average of 18.2 minutes. A power-law fit to the flare duration is also shown in Figure 7. A negative power-law index, p, of 2.2 ± 0.1 was found. This value is close to the value of 2.17 ± 0.05 found by Crosby et al. (1993) above 25 keV. Bromund et al. (1995) found larger values (2.40–2.94 depending on threshold) for >26 keV events as observed by the *International Cometary Explorer* (*ISEE 3*/*ICE*). A steepening of the power-law slope can be seen at large flare duration. This effect is most likely due to the requirement that *RHESSI*'s shutters remain out, which reduces the total number of large and therefore long-duration flares (see Fig. 9). Also note that a limit on the observed total flare duration exists due to *RHESSI*'s orbit, which is ~1 hr. In the same figure are histograms of the rise and decay durations. The average decay time is 3.71 minutes, and the average rise time is 2.25 minutes. The decay times are generally larger then the rise times, consistent with impulsive heating. Drake (1971) found a similar result: decay times (12 minutes) longer than rise times (4 minutes).

In order to characterize the impulsive or gradual nature of these flare events further, we consider the event asymmetry index, $A_{\rm ev}$, defined as

$$A_{\rm ev} = \frac{t_{\rm decay} - t_{\rm rise}}{t_{\rm decay} + t_{\rm rise}}; \tag{1}$$

it is a good measure of the temporal nature of flare events. Applied to Hα flares by Temmer et al. (2001) the event asymmetry index is a dimensionless quantity in the range [−1,+1], where values above zero imply an impulsive profile ($t_{\rm rise} < t_{\rm decay}$) while positive values imply the opposite ($t_{\rm rise} > t_{\rm decay}$). Figure 8 shows the distribution of event asymmetries. It is found that most flares are impulsive, with a mean asymmetry of −0.2, meaning that the flare peak occurs at ~40% of the flare duration. Some microflares are found to have a gradual rise (26%), although such a situation may be due to flares overlapping in time with a second flare occurring during the decay period of the first. In order to remove such cases, a subset of microflares was created through the requirement that the background before and after the flare is similar (the difference in backgrounds is less than 10% of the average), reducing the total number of flares to 3760. This reduction reduces the number of gradual rise microflares to 18% of the total and sharpens the distribution significantly yet does not significantly change the mean asymmetry.

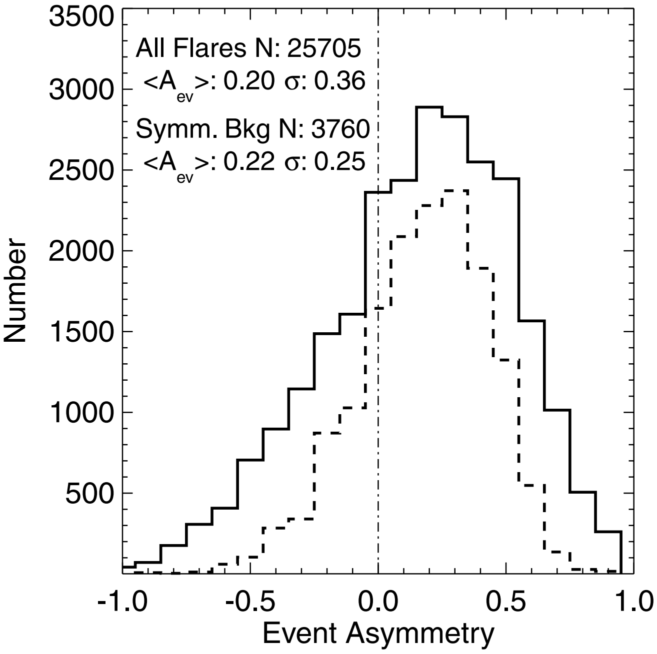

FIG. 8.—Histogram of the event temporal asymmetry, $A_{\rm ev} = (t_{\rm decay} - t_{\rm rise})/(t_{\rm decay} + t_{\rm rise})$. The dash-dotted line represents perfectly symmetric flares. Most flares are found to be impulsive (73%). The dashed histogram represents only those flares whose background count rate before and after are similar, so-called symmetric flares. This selection excludes flares which occur during the decay phase of other flares. The distribution of events is more clearly impulsive (81%), yet the mean event asymmetry remains the same.

Figure 9 shows the scatter plot of the characteristic times, total duration, $t_{\rm rise}$, and $t_{\rm decay}$, as a function of peak flux in the 6–12 keV range. This same energy range is used to determine the flare duration and consists of mostly thermal emission. We find a correlation coefficient in log-log space of 0.55 with a spread of 1 order of magnitude in duration. This is not unexpected, as larger flares heat more material and take longer to cool. Previous work by Veronig et al. (2002) using *GOES* (thermal) found a low correlation coefficient of ~0.25. We also find a correlation between the peak flux and rise or decay time. The correlation coefficients are 0.46 and 0.40 for rise and decay time, respectively. A simple interpretation of the correlation between flux and rise/decay time is that the slope of the rise/decay is roughly constant for all flares, meaning that the corona responds to heating and cooling through a fixed rate of change.

3.3. *Flare Frequency Distributions*

The occurrence frequency distribution, dN/dS, of peak flux for solar X-ray bursts has been known for some time to follow a power-law distribution of the form

$$\frac{dN}{dS} \propto W^{-\alpha}, \tag{2}$$

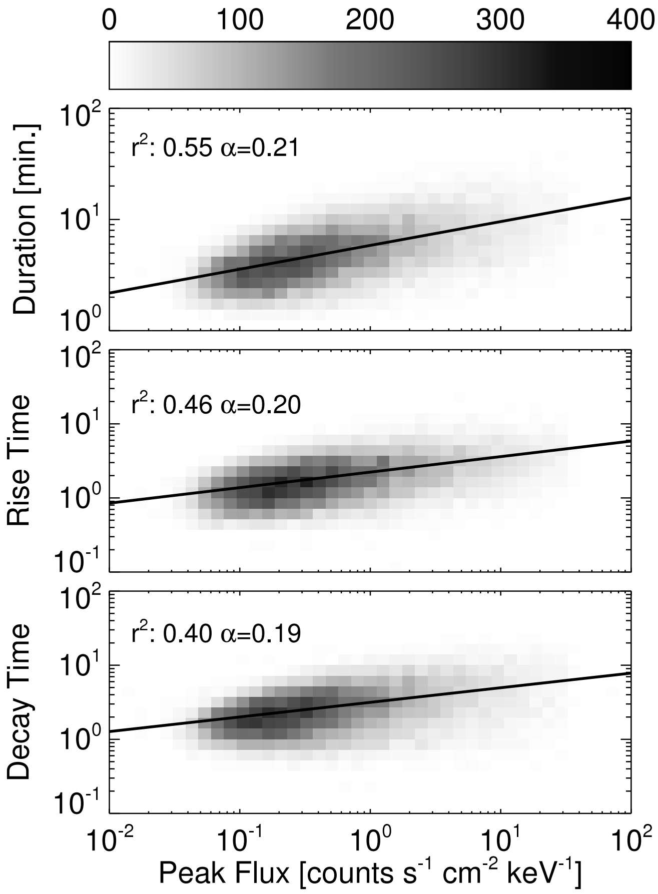

FIG. 9.—Flare duration as a function of peak flux in the 6–12 keV energy. The color bar shows the density of the number of microflares. The solid line represents the linear regression fit in log-log space to the data. The correlation coefficient and slopes are (*top*) 0.55 and 0.21 ± 0.01, (*middle*) 0.46 and 0.20 ± 0.20, and (*bottom*) 0.40 and 0.19 ± 0.01. [*See the electronic edition of the Journal for a color version of this figure.*]

where W is the peak flux (Datlowe et al. 1974; Drake 1971). Many studies have confirmed this fact (see Lin et al. 2001), reporting power-law indices between -1.5 and 2. Here we present the peak count rate distributions in different energy bands (Fig. 10). Although the distribution of total energy released is preferred in order to evaluate the microflare contribution to coronal heating, the energy of a flare is not an observable quantity, and its determination must rely on arbitrary assumptions (see § 3.4 and Paper II). It is therefore instructive to first consider the flux distribution. The frequency distributions presented here are corrected for instrumental effects using OSPEX, an updated version of the SPEX analysis package (Schwartz 1996).

Each frequency distribution, 3–6, 6–12, and 12–25 keV, can be represented by a power law over approximately 2 orders of magnitude. The low-energy band, 3–6 keV, contains thermal emission, while the 12–25 keV band is mostly nonthermal. The 6–12 keV band contains a mixture of both thermal and nonthermal counts but is dominated by thermal. The turnover at low fluxes is due to the fact that smaller events are more difficult to find and at high fluxes, flares are more likely to trigger the shutter and so are missing from this list. A linear fit to a range of the data in log-log space gives the following negative slopes for each energy band: 1.50 ± 0.03, 1.51 ± 0.03, and 1.58 ± 0.02, respectively. The errors are statistical and are smaller than the unknown systematic errors. The data ranges for the fit were chosen to minimize the χ^2 statistic. The slight increase in power-law index suggests that the indices may differ between thermal and nonthermal emission. The 12–25 keV band agrees best with the slope found by Crosby et al. (1993; 1.59 ± 0.04) for >25 keV. In Figure 10 (*lower right*), the unnormalized frequency histogram in the 6–12 keV energy range is plotted for different years. From 2002 to 2006 we find that the slope does not change significantly as a function of year within the solar cycle (Kucera et al. 1997), although, as expected, the total number of flares decreases with increasing year.

3.4. *Spectral Analysis*

Based on the spectra shown by Krucker et al. (2002), Benz & Grigis (2002), and in Paper II, microflare spectra are well represented by a power law of the form $F = A\epsilon^{-\gamma}$ above a break energy, $\epsilon_0 \approx 10$ keV, and therefore likely to be nonthermal, although this is difficult to determine unambiguously. Using count spectra at the 6–12 keV peak time integrated over 16 s, we estimated the power-law index by considering the ratio between 10–15 and 15–20 keV background-subtracted count rates. Since the thermal (6–12 keV) and nonthermal peak may not coincide in time, the nonthermal power-law index may be affected along with the derived energy. Single power-law photon spectra were convolved with the diagonal *RHESSI* response (Smith et al. 2002) to obtain the ratio of the 10–15 keV to the 15–20 keV for a range of power-law indices, γ. A histogram of the power-law indices can be seen in Figure 11, where the set of microflares is reduced to 16,463 events due to high pre-event backgrounds. The ratio of 10–15 to 15–20 keV channels is generally consistent with power-law indices between 4 and 12 (90% of events), although steeper power laws are also observed. The median index is 7.9, while the mean is 7.4, with a standard deviation of 2.7. These values are consistent with those found for individual events by Krucker et al. (2002) and Benz & Grigis (2002) but are markedly steeper than those for ordinary flares (e.g., Dennis 1985). In order to reproduce such steep spectra in this energy range with thermal emission requires high temperatures. Interpreted as thermal emission a power-law slope of 5 requires a temperature of 50 MK, while shallower slopes mean even higher temperatures. Such temperatures are not observed at low energies (3–10 keV; Paper II). Although it is difficult to unambiguously differentiate steep nonthermal emission from thermal emission, we shall assume all emission above 10 keV to be nonthermal in the following calculations.

Assuming that accelerated electrons lose their energy primarily through Coulomb collisions, then the energy loss rate, P, by electrons above an energy cutoff, E_C (in keV), is estimated by

$$P = 9.5 \times 10^{24}\gamma^2(\gamma - 1)\beta\left(\gamma - \frac{1}{2}, \frac{3}{2}\right)AE_C^{-\gamma+1} \text{ erg s}^{-1}, \qquad (3)$$

where $\beta(m, n)$ is the beta function (Brown 1971; Lin et al. 2001). Using the power-law indices shown in Figure 11 and setting a low and high cutoff to the power-law indices of 4 and 12 (reducing the total number of events to 14,237), respectively, the occurrence frequency of the power at the peak time is shown in Figure 11. Error analysis reduces the set of events with statistically significant values for the power down to 4241, assuming $E_C =$ 15 keV. Powers were calculated assuming $E_C = [10, 15, 25]$ keV, using equation (3). A 25 keV cutoff, although not consistent with how the photon spectral index was calculated, is included for comparison with previous studies such as Crosby et al. (1993). Based on previously observed microflares such as those presented in Krucker et al. (2002) or Benz & Grigis (2002) and Paper II, where the photon spectrum is fit including the energy

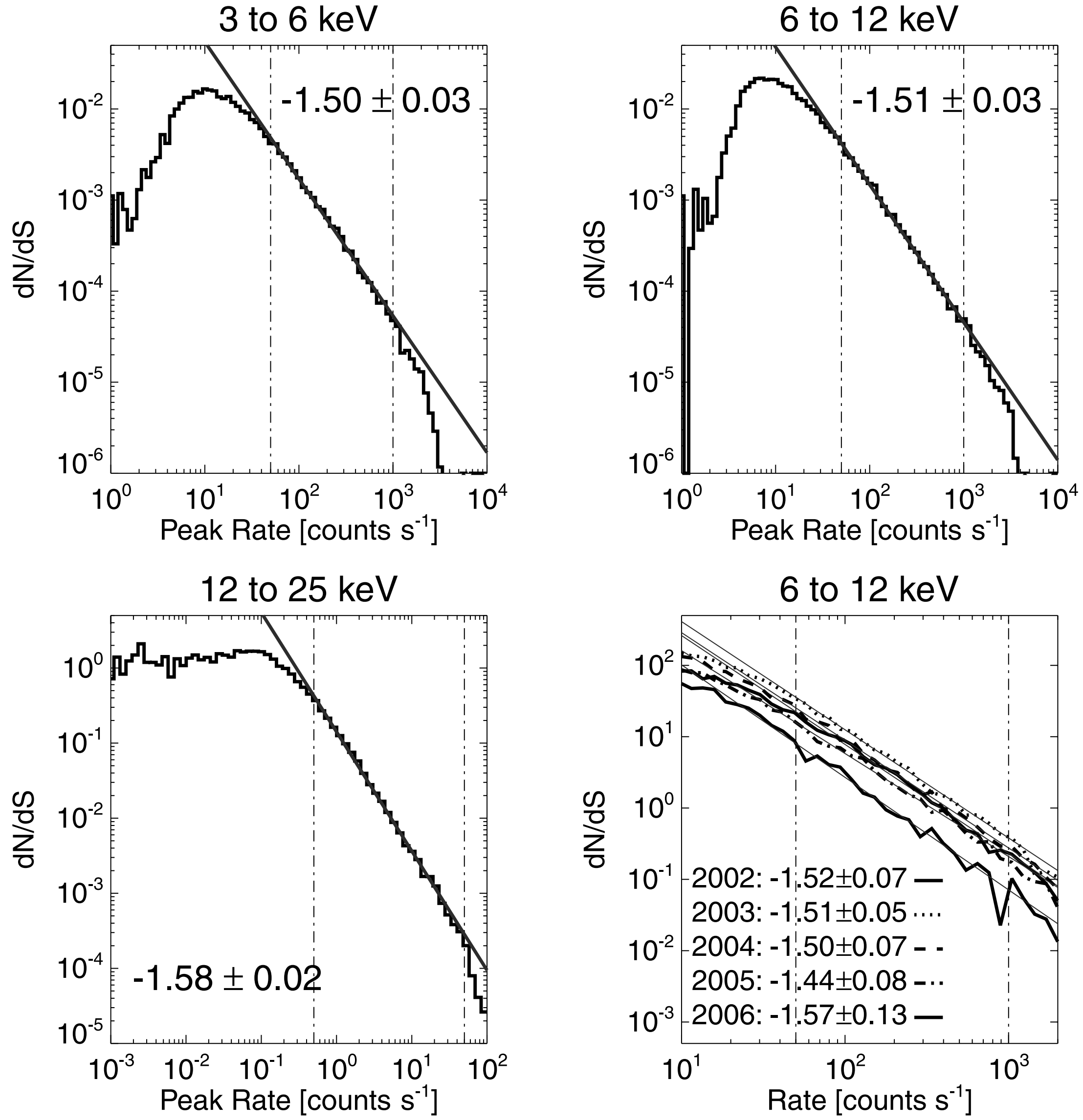

FIG. 10.—Histogram of the occurrence frequency of the peak count rate in three channels (3–6, 6–12, and 12–25 keV). Each can be fit by a power-law distribution. The fitted slope for each is shown along with the errors. The dash-dotted line represents the range of the fit. *Bottom right*: The 6–12 keV frequency distribution as a function of year. The distributions are not normalized in order to see the variation in flaring rates for different years.

cutoff and the median value for the energy cutoff was found to be 12.1 keV, the value $E_C = 15$ keV is most likely. Each distribution was fit using the maximum-likelihood method described by Parnell & Jupp (2000). This technique uses a maximum likelihood estimation to fit a skew-Laplace distribution, which consists of a broken power law, to the data. The advantage of this method is that it is independent of bin size and fits the turnover in the distribution. All of the distributions were found to be consistent with a power-law distribution with an index of -1.7 ± 0.1, where the error represents the range of indices for different values of E_C. A linear fit in log-log space is consistent with this result. This value agrees with Crosby et al. (1993), who found a value of 1.67 ± 0.04 for the frequency distribution of the peak power for much larger flares observed above 25 keV. Simulations of a distribution of low-energy cutoffs lead to a flattening of the distribution. The measured distribution is found to deviate from a power law at high and low powers due to selection effects. As noted by Krucker et al. (2002) for low values of E_C, the powers in accelerated electrons in microflares are comparable to those reported by Crosby et al. (1993) for flares observed above 25 keV. Although these microflares are rarely observed above 25 keV and would not have been included in the Crosby et al. (1993) study, the distributions have similar slopes, suggesting that *RHESSI* microflares are similar to large flares.

In order to determine the total energy content in nonthermal electrons in flares, the power must be integrated over the total duration of the nonthermal emission. Since this study is concerned with the smallest detectable events, analyzing spectra at times other than during the maximum count rate is difficult, but flare durations are available for every flare. Since the count spectra used to determine the power are averaged over 16 s, using this timescale results in a lower limit for the nonthermal energy. Assuming $E_C = 15$ keV, the calculated energies span 10^{28}–10^{30} erg, with a median value of 10^{28} erg. Using the rise time, $t_{\rm rise}$, an appropriate timescale, leads to energies between 10^{29} and 10^{31} erg and a median energy of 10^{29} erg. These values are very sensitive to the choice of the low-energy cutoff, E_C, and should be considered maximum values. Assuming a cutoff of 10 keV increases

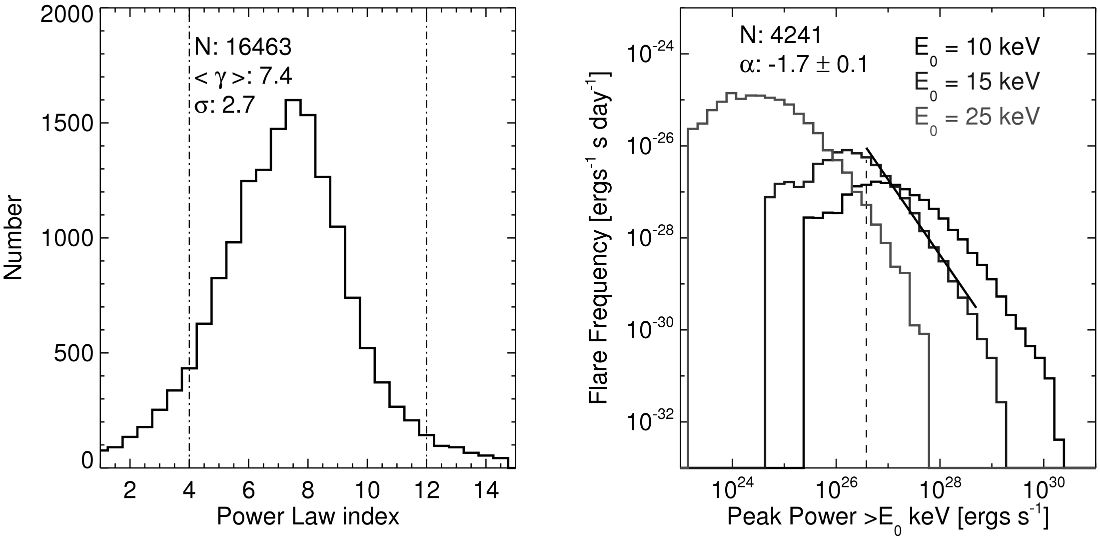

FIG. 11.—*Left*: Histogram of the power-law index. The average power-law index is 7.4. The standard deviation of the distribution is 2.7. The vertical lines represent the range used in determining the power in nonthermal electrons. *Right*: The power distribution of *RHESSI* flares in greater than $E_C = [10, 15, 25]$ keV accelerated electrons. Error analysis reduces the number of events to 4241. Each distribution was fit using the maximum likelihood method by Parnell & Jupp (2000), which returns a slope and a cutoff (*dashed vertical line*). The fit results for $E_C = 15$ keV are illustrated, and the power slope is found to be 1.7 ± 0.1. The error represents the range of fitted slopes from $E_C = 10$ and 25 keV. [*See the electronic edition of the Journal for a color version of this figure.*]

these values by 1 order of magnitude. These energies are comparable to the large flares observed by Crosby et al. (1993) yet if the same low-energy cutoff is assumed (25 keV), then the microflare energies are smaller, on average, by a factor of $\sim$100.

Since these microflares are active region related, they cannot heat the quiet-Sun corona, but the total energy in microflare-accelerated nonthermal electrons may still be relevant to the heating of active regions. We find that the rate of energy released by these microflares is less than 10^{26} erg s^{-1} averaged over the total 5 yr of observations. This value is similar to that found by Lin et al. (2001), who considered similarly sized events. Withbroe & Noyes (1977) estimated the energy flux required to maintain the temperature of active regions to be 10^7 erg cm^{-2} s^{-1}. This values includes radiative, conductive, and kinetic losses. Using an average active region area of 10^{20} cm^2, the microflares contribute at most 10% of the required energy to heat the active region corona. It should be noted that the microflare contribution to the active region corona is impulsive and provides energy only during roughly 30% (2%) of the time during solar maximum (minimum). Other times have no detectable energy input by microflares into the active region corona. This suggests that a more frequent energy input is present in addition to microflares.

4. SUMMARY AND CONCLUSION

Considering a total of 5 yr of observations, a newly developed flare-finding algorithm found 25,705 *RHESSI* microflares of which 24,097 could be imaged. Microflares are impulsive in nature with rise times shorter than decay times, and larger microflares have longer durations. These microflares range from *GOES* A to B class events (background-subtracted), are well correlated with solar activity, and occur only in active regions, rather than in the quiet Sun. This is not unexpected, as Hannah et al. (2007) showed the HXR flux (3–200 keV) from the quiet Sun to be at least 2 orders of magnitude smaller than that of observed microflares. This suggests that energy releases in the quiet Sun have a nonthermal energy threshold below 10^{28} erg, assuming a low-energy cutoff of 15 keV. Observations of bursts in the quiet Sun have estimated the thermal energy to be between 10^{24} and 10^{26} erg (Krucker & Benz 1998; Parnell & Jupp 2000).

Assuming nonthermal emission above 15 keV, we conclude that microflare spectra are generally steep with a mean spectral index of -7.4 and that the power distribution, regardless of assumed E_C, is consistent with that of large flares, distributed as a power law with a slope of 1.7 ± 0.1. We therefore conclude that *RHESSI* microflares are similar to large flares. The fact that our microflare energies (assuming $E_C = 15$ keV) are comparable to those (25 keV) flares analyzed in earlier studies suggests that previous flare energies may have been systematically underestimated due to a lack of knowledge of the low-energy cutoff. This may also be true of energy estimates of large flares observed by *RHESSI*. In this case, the low-energy cutoff may be hidden by thermal emission. Another possibility may be that the microflare nonthermal energy presented in this paper is being overestimated, which may require our interpretation of nonthermal emission as collisional bremsstrahlung of fast electrons on ions (so-called free-free emission) to be revised. As suggested by Brown & Mallik (2007), recombination radiation (free-bound emission), where fast electrons are captured by ions, is most important at low energies and for steep spectra and may be important in microflares. Its inclusion could reduce the nonthermal energy in microflares by up to a factor of $\sim$10. However, free-bound emission is only important in high-temperature plasmas, which may not be present in microflares. A reconsideration of the standard thick-target interpretation may be necessary in order to derive a consistent flare energy distribution.

This work was supported under NASA grant NAS5-98033, NNG05GG16G, and NNM05ZA12H. S. Christe would like to thank H. Hudson, G. Hurford, and A. Y. Shih for helpful discussions. The authors would also like to thank the referee for a critical reading of the manuscript. This research has made use of NASA's Astrophysics Data System.

REFERENCES

Aschwanden, M. J., Nightingale, R. W., & Alexander, D. 2000, ApJ, 541, 1059

Battaglia, M., Grigis, P. C., & Benz, A. O. 2005, A&A, 439, 737

Benz, A. O., & Grigis, P. C. 2002, Sol. Phys., 210, 431

Benz, A. O., & Krucker, S. 2002, ApJ, 568, 413

Bromund, K. R., McTiernan, J. M., & Kane, S. R. 1995, ApJ, 455, 733

Brown, J. C. 1971, Sol. Phys., 18, 489

Brown, J. C., & Mallik, P. C. V. 2007, A&A, in press (arXiv:0706.2823B)

Crosby, N. B., Aschwanden, M. J., & Dennis, B. R. 1993, Sol. Phys., 143, 275

Crosby, N. B., Vilmer, N., Lund, N., & Sunyaev, R. 1998, A&A, 334, 299

Datlowe, D. W., Elcan, M. J., & Hudson, H. S. 1974, Sol. Phys., 39, 155

Dennis, B. R. 1985, Sol. Phys., 100, 465

Drake, J. F. 1971, Sol. Phys., 16, 152

Feldman, U., Doschek, G. A., Behring, W. E., & Phillips, K. J. H. 1996, ApJ, 460, 1034

Hannah, I. G., Christe, S., Krucker, S., Hurford, G. J., Hudson, H. S., & Lin, R. P. 2008, ApJ, 677, 704

Hannah, I. G., Hurford, G. J., Hudson, H. S., Lin, R. P., & van Bibber, K. 2007, ApJ, 659, L77

Hurford, G. J., et al. 2002, Sol. Phys., 210, 61

Krucker, S., & Benz, A. O. 1998, ApJ, 501, L213

Krucker, S., Benz, A. O., Bastian, T. S., & Acton, L. W. 1997, ApJ, 488, 499

Krucker, S., Christe, S., Lin, R. P., Hurford, G. J., & Schwartz, R. A. 2002, Sol. Phys., 210, 445

Krucker, S., & Lin, R. P. 2008, ApJ, 673, 1181

Kucera, T. A., Dennis, B. R., Schwartz, R. A., & Shaw, D. 1997, ApJ, 475, 338

Lin, R. P., Feffer, P. T., & Schwartz, R. A. 2001, ApJ, 557, L125

Lin, R. P., Schwartz, R. A., Kane, S. R., Pelling, R. M., & Hurley, K. C. 1984, ApJ, 283, 421

Lin, R. P., et al. 2002, Sol. Phys., 210, 3

Liu, C., Qiu, J., Gary, D. E., Krucker, S., & Wang, H. 2004, ApJ, 604, 442

Lu, E. T., & Hamilton, R. J. 1991, ApJ, 380, L89

Lu, E. T., Hamilton, R. J., McTiernan, J. M., & Bromund, K. R. 1993, ApJ, 412, 841

Maunder, E. W. 1904, MNRAS, 64, 747

Parker, E. N. 1988, ApJ, 330, 474

Parnell, C. E., & Jupp, P. E. 2000, ApJ, 529, 554

Qiu, J., Liu, C., Gary, D. E., Nita, G. M., & Wang, H. 2004, ApJ, 612, 530

Schwartz, R. 1996, NASA STI/Recon Tech. Rep. N (Greenbelt: NASA), 71448

Shimizu, T. 1995, PASJ, 47, 251

Smith, D. M., et al. 2002, Sol. Phys., 210, 33

Stoiser, S., Veronig, A. M., Aurass, H., Hanslmeier, A. 2007, Sol. Phys., 246, 339

Su, Y., Gan, W. Q., & Li, Y. P. 2006, Sol. Phys., 238, 61

Temmer, M., Veronig, A., Hanslmeier, A., Otruba, W., & Messerotti, M. 2001, A&A, 375, 1049

Veronig, A., Temmer, M., Hanslmeier, A., Otruba, W., & Messerotti, M. 2002, A&A, 382, 1070

Wheatland, M. S. 2001, Sol. Phys., 203, 87

Withbroe, G. L., & Noyes, R. W. 1977, ARA&A, 15, 363